Frequency-Selective MEMS for Miniaturized Low-Power Communication Devices

Clark T.-C. Nguyen, *Member, IEEE*

(Invited Paper)

Abstract— With Q's in the tens to hundreds of thousands, micromachined vibrating resonators are proposed as integrated-circuit-compatible tanks for use in the low phase-noise oscillators and highly selective filters of communications subsystems. To date, LF oscillators have been fully integrated using merged CMOS/microstructure technologies, and bandpass filters consisting of spring-coupled micromechanical resonators have been demonstrated in a frequency range from HF to VHF. In particular, two-resonator micromechanical bandpass filters have been demonstrated with frequencies up to 35 MHz, percent bandwidths on the order of 0.2%, and insertion losses less than 2 dB. Higher order three-resonator filters with frequencies near 455 kHz have also been achieved, with equally impressive insertion losses for 0.09% bandwidths, and with more than 64 dB of passband rejection. Additionally, free-free-beam single-pole resonators have recently been realized with frequencies up to 92 MHz and Q's around 8000. Evidence suggests that the ultimate frequency range of this high-Q tank technology depends upon material limitations, as well as design constraints, in particular, to the degree of electromechanical coupling achievable in micro-scale resonators.

Index Terms— Bandpass, communications, filter, fabrication, low power, MEMS, microelectromechanical devices, micromachining, micromechanical, transceiver, oscillators, resonators.

I. INTRODUCTION

VIBRATING mechanical tank components, such as crystal and SAW resonators, are widely used for frequency selection in communication subsystems because of their high quality factor (Q's in the tens of thousands) and exceptional stability against thermal variations and aging. In particular, the majority of heterodyning communication transceivers rely heavily upon the high-Q of SAW and bulk acoustic mechanical resonators to achieve adequate frequency selection in their RF and IF filtering stages and to realize the required low phase noise and high stability in their local oscillators. Currently, such mechanical resonator tanks are off-chip components and, thus, must interface with integrated electronics at the board level, often consuming a sizable portion of the total subsystem area. In this respect, these devices pose an important bottleneck against the ultimate miniaturization and portability of wireless

transceivers. For this reason, many research efforts are focused upon strategies for either miniaturizing these components [1]–[5] or eliminating the need for them altogether [6]–[8].

Recent demonstrations of micro-scale high-Q oscillators and mechanical bandpass filters with area dimensions on the order of 30 μm × 20 μm now bring the first of the above strategies closer to reality [9], [10]. Such devices utilize high-Q on-chip micromechanical (hereafter referred to as "μmechanical") resonators [11], [12] constructed in polycrystalline silicon using integrated-circuit (IC) compatible surface micromachining fabrication techniques, and featuring Q's of over 80 000 [13] under vacuum and center frequency temperature coefficients in the range of −10 ppm/°C (several times less with nulling techniques) [14]. To date, two-resonator micromechanical bandpass filters have been demonstrated with frequencies up to 35 MHz, percent bandwidths on the order of 0.2%, and insertion losses less than 2 dB [9], [15]–[18]. Higher order three-resonator filters with frequencies near 455 kHz have also been achieved, with equally impressive insertion losses for 0.09% bandwidths, and with more than 64 dB of passband rejection [19]. LF (i.e., 20 kHz) high-Q oscillators, fully-integrated with sustaining CMOS electronics, have also been demonstrated in this technology [20]–[22].

For use in many portable communications applications, however, higher frequencies must be achieved. Thus, frequency extension into the higher VHF and UHF ranges is currently the subject of ongoing research. This paper presents an overview of recent advances in frequency-selective micro-electromechanical systems (MEMS) devices aimed at both size reduction and performance enhancement of transceivers via miniaturization of high-Q signal-processing elements. Specific results will be reported, including a review of integrated oscillator work and of recently demonstrated micromechanical resonators and filters in the VHF range. The remainder of this paper will then focus upon projections for the ultimate frequency range and performance of these communications devices.

II. ADVANTAGES OF MEMS

Reduced size constitutes the most obvious incentive for replacing SAW's and crystals by equivalent μmechanical devices. The substantial size difference between microme-chanical resonators and their macroscopic counterparts is illustrated in Fig. 1, which compares a typical SAW resonator with a clamped–clamped beam micromechanical resonator of

The author is with the Department of Electrical and Computer Engineering Department, The University of Michigan at Ann Arbor, Ann Arbor, MI 48109-2122 USA.

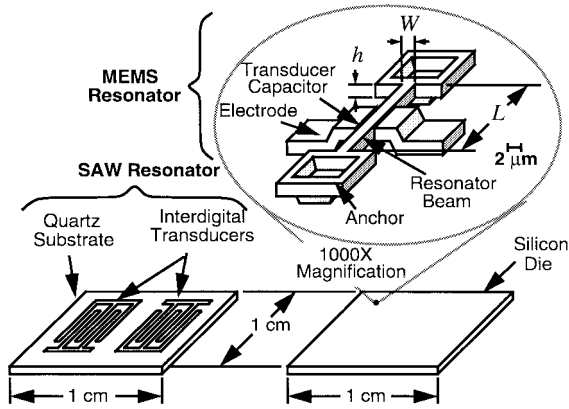Publisher Item Identifier S 0018-9480(99)06087-1.

Fig. 1. Size comparison between present-day SAW resonator technology and the described high-Q μmechanical resonator technology.
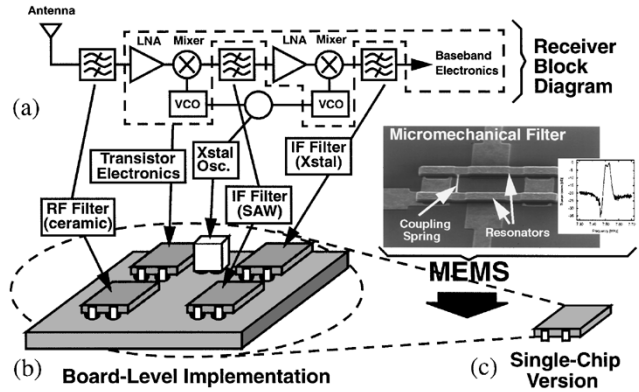

Fig. 2. (a) Simplified block diagram of a dual-conversion receiver. (b) Approximate physical implementation, emphasizing the board-level nature (many inductor and capacitor passives not shown). (c) Possible single-chip implementation using MEMS technology.

comparable frequency. The particular μresonator shown is excited electrostatically via parallel-plate capacitive transducers and designed to vibrate in a direction parallel to the substrate with a frequency determined by material properties, geometric dimensions, and stress in the material. Typical dimensions for a 100-MHz micromechanical resonator are $L \approx 12.9 \, \mu$m, $W = 2 \, \mu$m, and $h = 2 \, \mu$m. With electrodes and anchors, this device occupies an area of $420 \, \mu$m$^2 = 0.00042 \, \mu$m^2. Compared with the several mm^2 required for a typical VHF-range SAW resonator, this represents several orders of magnitude in size reduction.

A related incentive for the use of micromechanics is integrability. Micromechanical structures can be fabricated using the same planar process technologies used to manufacture integrated circuits. Several technologies demonstrating the merging of CMOS with surface micromachining have emerged in recent years [21], [23], [24], and one of these is now used for high-volume production of commercial accelerometers [23]. Using similar technologies, complete systems containing integrated micromechanical filters and oscillator tanks, as well as amplification and frequency translation electronics, all on a single chip, are possible. This, in turn, makes possible high-performance single-chip transceivers with heterodyning architectures and all the communication link advantages associated with them. Other advantages inherent with integration are also obtained, such as elimination of board-level parasitics that could otherwise limit filter rejections and distort their passbands.

A. High-Q MEMS for Transceiver Miniaturization

The front-end of a wireless transceiver typically contains a good number of off-chip high-Q components that are potentially replaceable by micromechanical versions. Among the components targeted for replacement are RF filters, including image reject filters, with center frequencies ranging from 800 MHz to 2.5 GHz; IF filters, with center frequencies ranging from 455 kHz to 254 MHz; and high-Q low phase-noise local oscillators with frequency requirements in the 10-MHz–2.5-GHz range. Fig. 2 summarizes the high-Q components potentially replaceable by micromechanical versions in a simplified superheterodyne receiver architecture

and illustrates the possibility for shrinking present-day board-level receiver implementations to single-chip ones via MEMS technology.

B. Power Savings via MEMS

Although certainly a significant advancement, miniaturization of transceivers only touches the surface of the true potential of this technology. MEMS technology may, in fact, make its most important impact not at the component level, but at the system level, by offering alternative transceiver architectures that emphasize selectivity over complexity to substantially reduce power consumption and enhance performance.

The power-savings advantages afforded by MEMS is perhaps best illustrated by comparison with recent attempts to reduce the cost and size of wireless transceivers via increased circuit complexity. Specifically, in these approaches, higher levels of transistor integration and alternative architectures are used to reduce the need for the off-chip high-Q passives used in present-day superheterodyne transceivers, with obvious size advantages. Unfortunately, removal of off-chip passives often comes at the cost of increased power consumption in circuits preceding and including the analog-to-digital converter (ADC), which now must have higher dynamic ranges to avoid intermodulation distortion and desensitization caused by larger adjacent channel interferers. A selectivity (or Q) versus power tradeoff is clearly seen here.

To better convey this point, specific phenomena that comprise the spurious-free dynamic range (SFDR) of a receiver are illustrated in Fig. 3(a), which depicts the signal flow from antenna to baseband for a desired signal at ω_{inf} with two adjacent interferers (offset $\Delta\omega$ and $2\Delta\omega$) assuming a conventional receiver architecture using *wide-band* RF filters. As shown, due to nonlinearity in various components (e.g., the low-noise amplifier (LNA), mixer, A/D converter) and phase noise in the local oscillator, the presence of interferers can potentially desensitize the receiver by: 1) generating third-order intermodulation (IM_3) distortion components over the desired signal at the outputs of various components (The LNA is depicted as the culprit in Fig. 3(a) for clarity, but succeeding stages could also very easily dominate this effect.)
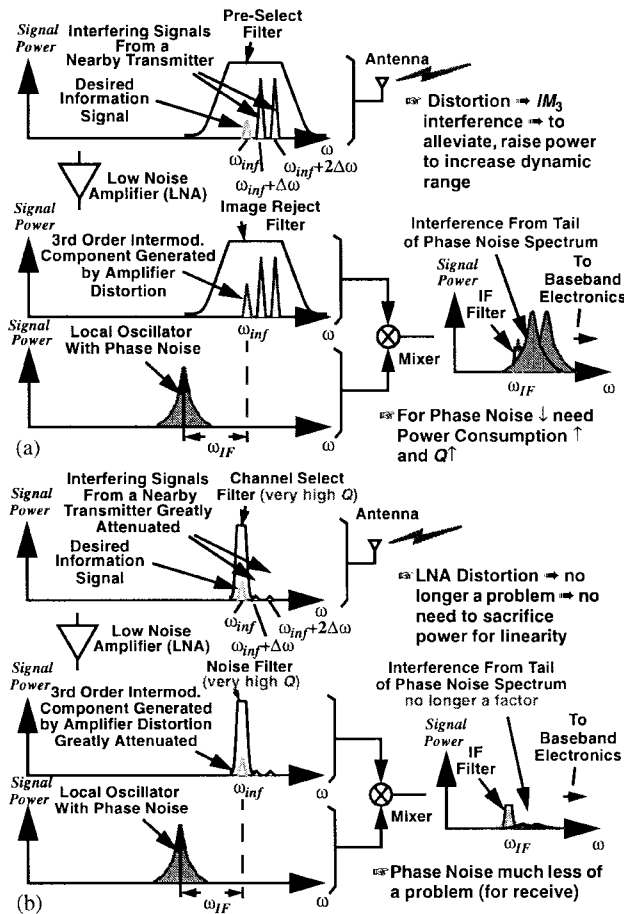
Fig. 3. Modified signal flow diagrams for: (a) conventional receiver using wide-band RF filters and (b) RF channel-select receiver.
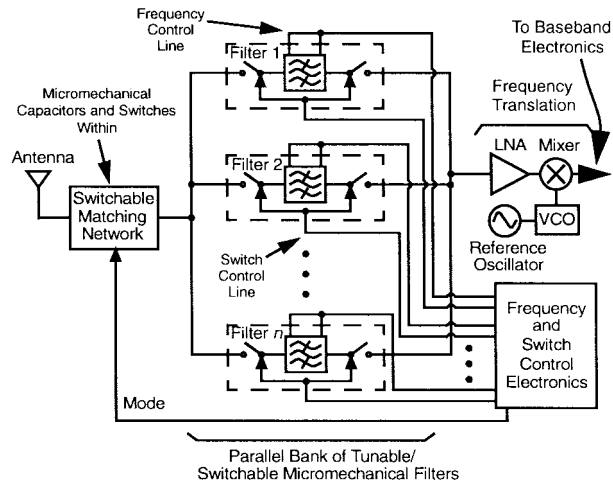

Fig. 4. Possible front-end receiver architecture utilizing a parallel bank of tunable/switchable micromechanical filters for a first stage of channel selection. Note that several micromechanical resonator devices can also be used within the frequency translation blocks as well.

and 2) aliasing superposed phase-noise sidebands from the local oscillator onto the desired signal immediately after the mixer stage. In order to avoid such interference, components in the signal path must satisfy a strict linearity (or dynamic range) requirement, and the local oscillator a strict phase-noise requirement, both of which often demand significantly higher power consumption in these components.

A method for eliminating such a waste of power becomes apparent upon the recognition that the above interference phenomena arise in conventional architectures only because such architectures allow adjacent-channel signals to pass through the RF filter and reach the LNA and mixer. If these signals were instead eliminated at the outset by a much more selective RF filter, then interference from IM_3 components and from phase-noise sidebands would be greatly alleviated, as shown in Fig. 3(b), and specifications on linearity and phase noise could be greatly relaxed. The use of such a filtering strategy may be limited by group delay requirements in some pulse modulation schemes, but where usable, the power savings afforded by such relaxations in active component specifications can be substantial. The above discussion pertains to the receive path, but if channel-select filters with both sufficiently high Q and power handling capability are available and placed right before the transmitting antenna, similar power savings are possible for the *transmit* local oscillator and power amplifier as well.

An architecture such as that shown in Fig. 3(b) requires a tunable highly selective (i.e., high-Q) filter capable of operation at RF frequencies. Unfortunately, partially due to their own high stability, high-Q filters are generally very difficult to tune over large frequency ranges, and MEMS-based filters are no exception to this. Although μmechanical resonators can be tuned over larger frequency ranges than other high-Q tank technologies, with voltage-controllable tuning ranges of up to 5%, depending on design, a single micromechanical filter still lacks the tuning range needed for some wide-band applications.

Thanks to the tiny size of micromechanical filters, however, there no longer needs to be only one filter. One of the major advantages of micromechanical filters is that because of their tiny size and zero dc power dissipation, many of them (perhaps hundreds or thousands) can be fabricated onto a smaller area than occupied by a single one of today's macroscopic filters. Thus, rather than use a single tunable filter to select one of several channels over a large frequency range, a massively parallel bank of switchable micromechanical filters can be utilized, in which desired frequency bands can be switched in, as needed. The simplified block diagram for such a front-end architecture is illustrated in Fig. 4, where each filter switch combination corresponds to a single micromechanical filter, with input and output switches activated by the mere application or removal of dc-bias voltages (V_P, in later discussions) from the resonator elements. By further exploiting the switching flexibility of such a system, some very resilient frequency-hopping spread spectrum transceiver architectures can be envisioned that take advantage of simultaneous switching of high-Q micromechanical filters and oscillators.

In effect, frequency-selective devices based on MEMS technologies can potentially enable substantial power savings by making possible paradigm-shifting transceiver architectures that, rather than eliminate high-Q passive components, attempt to maximize their role with the intention of harnessing the Q versus power tradeoff often seen in transceiver design. The
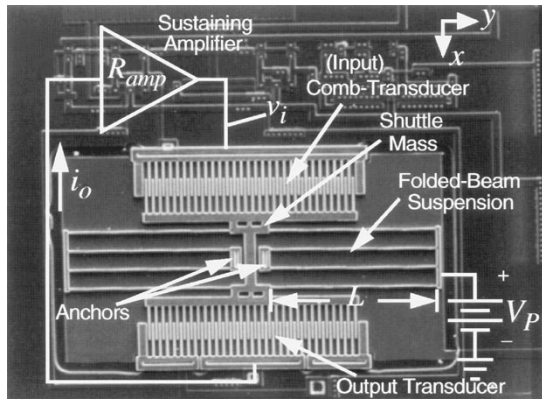
Fig. 5. SEM of a 16.5-kHz CMOS μresonator oscillator with schematics explicitly depicting circuit topology. The μresonator occupies 420×430 μm^2.

following sections of this paper now focus upon the subject micromechanical resonator devices.

III. MICROMECHANICAL RESONATOR OSCILLATORS

The scanning electron micrograph (SEM) for a 16.5-kHz micromechanical resonator oscillator, fully integrated with sustaining CMOS electronics, is shown in Fig. 5 [20]. To maximize frequency stability against supply voltage variations [20], [21] a folded-beam comb-transduced micromechanical resonator is utilized [11]. As shown, this μresonator consists of a finger-supporting shuttle mass suspended 2 μm above the substrate by folded flexures, which are anchored to the substrate at two central points. The shuttle mass is free to move in the x-direction indicated, parallel to the plane of the silicon substrate, with a fundamental resonance frequency determined largely by material properties and by geometry, given by [11]

$$f_o = \frac{1}{2\pi}\sqrt{\frac{k_{rs}}{m_{rs}}} = \frac{1}{2\pi}\left[\frac{2Eh(W/L)^3}{(M_P + \frac{1}{4}M_t + \frac{12}{35}M_b)}\right]^{1/2} \quad (1)$$

where m_{rs} and k_{rs} are the effective mass and stiffness at locations on the resonator shuttle, E is the Young's modulus of the structural material, M_P is the shuttle mass, M_t is the mass of the folding trusses, M_b is the total combined mass of the suspending beams, W and h are the cross-sectional width and thickness, respectively, of the suspending beams, and L is indicated in Fig. 5.

To properly excite this device, a voltage consisting of a dc-bias V_P and an ac excitation v_i is applied across one of the resonator-to-electrode comb capacitors (i.e., the input transducer). This creates a force component between the electrode and resonator proportional to the product $V_P v_i$ and at the frequency of v_i. When the frequency of v_i nears its resonance frequency, the μresonator begins to vibrate, creating a dc-biased time-varying capacitor $C_o(x,t)$ at the output transducer. A current given by

$$i_o = V_P \frac{\partial C_o}{\partial x}\frac{\partial x}{\partial t} \quad (2)$$

is then generated through the output transducer and serves as the output of this device. When plotted against the frequency
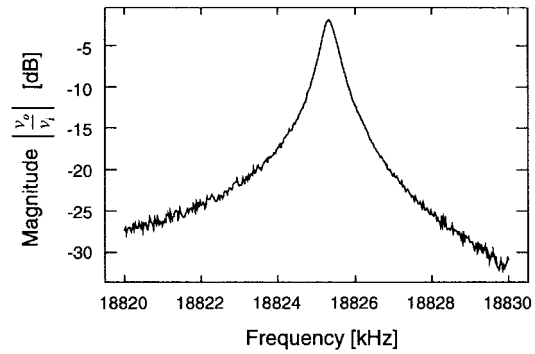

Fig. 6. Measured transconductance spectrum for a folded-beam capacitive-comb transduced polysilicon μmechanical resonator operated under a vacuum pressure of 20 mtorr. ($v_o = i_o R_f$, where R_f is the gain of a transresistance amplifier used for output current detection.)
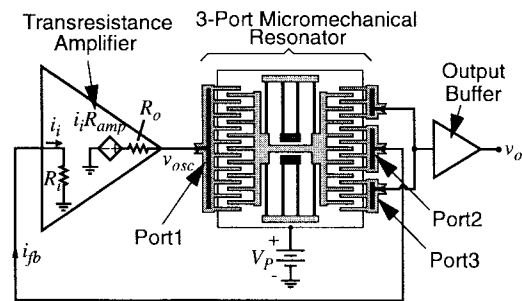

Fig. 7. System-level schematic for the μresonator oscillator of Fig. 5.

of the excitation signal v_i, the output current i_o traces out the bandpass biquad characteristic expected for a high-Q tank circuit. Fig. 6 presents the transconductance spectrum for the micromechanical resonator of Fig. 5, measured under 20-mtorr vacuum using a dc-bias V_P of 20 V and an excitation signal of 1-mV peak. From this plot, the extracted Q is approximately 50 000.

Note also, from the discussion associated with (2), that the effective input force ($\sim V_P v_i$) and output current can be nulled by setting $V_P = 0$ V. Thus, a micromechanical resonator (or filter constructed of such resonators) can be switched in and out by the mere application and removal of the dc-bias voltage V_P. As described in conjunction with Fig. 4, such switchability can be used to great advantage in receiver architectures.

A. Oscillator Design

A system-level schematic for the oscillator of Fig. 5 is shown in Fig. 7. As shown, this oscillator utilizes a three-port μmechanical resonator, for which two ports are embedded in a (zero phase shift) positive feedback loop in series with a sustaining transresistance amplifier, while a third port is directed to an output buffer. The use of a third port effectively isolates the sustaining feedback loop from variations in output loading.

For the purposes of start-up design, a small-signal equivalent circuit for the micromechanical resonator is useful. The small-signal equivalent circuit for the three-port micromechanical resonator of Fig. 7, obtained via an appropriate impedance analysis [20], is presented in Fig. 8, along with equations for
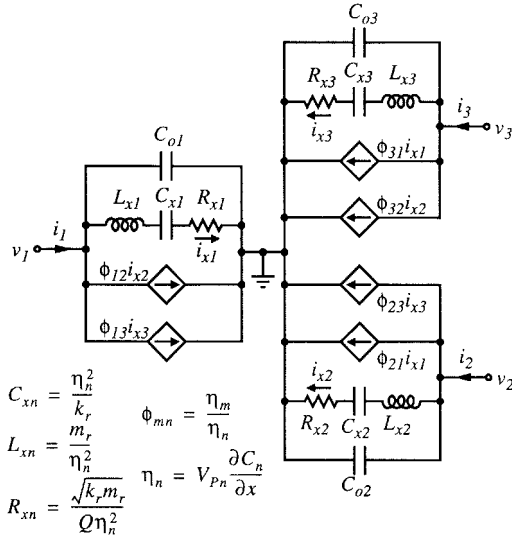
Fig. 8. Small-signal equivalent circuit for a three-port μmechanical resonator with equations for the elements. In the equations, m_r is the effective mass of the resonator at the shuttle location, k_r is the corresponding system spring constant, and $\partial C_n/\partial x$ is the change in capacitance per unit displacement at port n.

TABLE I
μmechanical RESONATOR DATA

Parameter	Value	Units
Folded-Beam Length, L	185.3	μm
Folded-Beam Width, W	1.9	μm
Structural Layer Thickness, h	2	μm
Effective Mass @ Shuttle, m_r	5.73×10^{-11}	kg
Effective Stiffness @ Shuttle, k_r	0.65	N/m
No. Finger Overlaps at Port 1, N_{g1}	60	—
No. Finger Overlaps at Port 2, N_{g2}	30	—
No. Finger Overlaps at Port 3, N_{g3}	30	—
Finger Gap Spacing, d	2	μm
Finger Overlap Length, L_d	20	μm
$\partial C/\partial x$ per Finger Overlap	9.74×10^{-12}	F/m
Measured Q at 20 mTorr	23,400	—
Young's Modulus, E [11]	150	GPa
Density of Polysilicon, ρ	2,300	kg/m^3
Calculated Resonance Frequency, f_o	16.9	kHz
Measured Resonance Frequency, f_o	16.5	kHz

each of the elements. As shown, the electrical impedances looking into each of the ports are modeled by *LCR* tanks in parallel with shunt capacitors C_{on}, while port-to-port coupling is modeled via current-controlled current sources. Details of the overall design and small-signal circuit model for the three-port μresonator of Fig. 5 are summarized in Tables I and II.

Assuming that the bandwidth of the sustaining transresistance amplifier is much larger than the oscillation frequency (so as to prevent excess phase shift at that frequency), oscillation start-up will occur when the loop gain A_l is larger than unity. For this series resonant oscillator design, the loop gain

TABLE II
μresonator EQUIVALENT-CIRCUIT ELEMENT VALUES*

Element	Port 1 ($n=1$)	Port 2 ($n=2$)	Port 3 ($n=3$)	Units
C_{on}	11.7	5.8	5.8	fF
C_{xn}	0.65	0.16	0.16	fF
L_{xn}	136.5	545.8	545.8	kH
R_{xn}	620.8	2483.1	2483.1	kΩ
ϕ_{mn}	$\phi_{12}=-2$	$\phi_{21}=-0.5$	$\phi_{31}=-0.5$	A/A
	$\phi_{13}=-2$	$\phi_{23}=1$	$\phi_{32}=1$	A/A

* Calculated using values in Table I and V_{Pn}=35V.

is given by

$$A_l = \frac{R_{\mathrm{amp}}}{R_{x12}+R_i+R_o} \quad (3)$$

where R_i is the input resistance of the transresistance amplifier, R_o is its output resistance, R_{amp} is its transresistance gain, and R_{x12} is the equivalent-series motional resistance between ports 1 and 2 of the μmechanical resonator, given by [20]

$$R_{x12} = -\frac{v_1}{i_2} = -\frac{R_{x1}}{\phi_{21}} = \frac{R_{x1}}{|\phi_{21}|} \quad (4)$$

where variables are defined in Fig. 8.

Conceptually, this oscillator may also be modeled as a negative-resistance oscillator, with the quantities $(-R_{\mathrm{amp}})$ and $(R_{x12} + R_i + R_o)$ comprising negative and positive resistances, respectively. During start-up, if $A_l > 1$, the negative (trans)resistance of the amplifier R_{amp} is larger in magnitude than the positive resistance $(R_{x12} + R_i + R_o)$, and oscillation results. Oscillation builds up until either some form of nonlinearity or a designed automatic-level control circuit alters either or both resistors so that $R_{\mathrm{amp}} = R_{x12}+R_i+R_o$, at which point $A_l = 1$ and the oscillation amplitude limits. Unlike many of its macroscopic counterparts, amplitude limiting of this oscillator ultimately arises from nonlinearity in the micromechanical resonator, not in the sustaining amplifier [20].

The transresistance sustaining amplifier in Fig. 5 utilizes a linear region MOS resistor in a shunt–shunt feedback configuration around an NMOS driver device to implement a gate voltage-controllable transresistance gain [20]. Using a 2-μm-channel length CMOS technology, the circuit achieves a bandwidth of 12.7 MHz when biased for a transresistance gain of 5.5 MΩ—sufficient gain and bandwidth to achieve practically zero-phase-shift oscillation when coupled with the μresonator of Tables I and II. The output circuit is a replica of the sustaining amplifier with added buffer electronics for driving off-chip loads. Circuit details for both amplifiers can be found in [20]. The total area consumed by the 16.5-kHz prototype oscillator of Fig. 5 is 420 $\times$ 330 μm^2. As will become apparent, higher frequency oscillators will require μresonators with much less mass and, thus, should occupy an even smaller area.

B. Fully Integrated Oscillator Fabrication

1) Surface Micromachining: A polysilicon surface micromachining technology [11], [12] was used to fabricate the
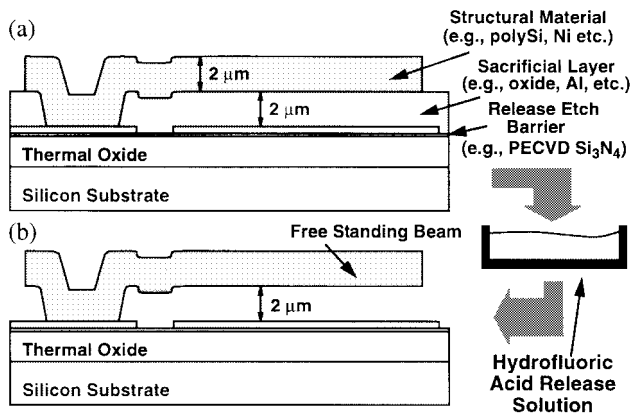
Fig. 9. Cross section depicting the fabrication sequence used to achieve micromechanical resonators. (a) Required film layers up to the release etch step. (b) Resulting freestanding beam following a release etch in hydrofluoric acid.

μmechanical resonator of this work. In this process, a series of film depositions and lithographic patterning steps—identical to similar steps used in planar fabrication technologies—are used to first achieve the cross section shown in Fig. 9(a). Here, a sacrificial oxide layer supports the structural polysilicon material during deposition, patterning, and subsequent annealing. In the final step of the process, the wafer containing cross sections similar to Fig. 9(a) is dipped into a solution of hydrofluoric acid, which etches away the sacrificial oxide layer without significantly attacking the polysilicon structural material. This leaves the freestanding structure shown in Fig. 9(b), capable of movement in three dimensions, if necessary.

2) Merging CMOS with Micromechanics: The technology for the fully monolithic high-Q oscillator of Fig. 5 combines planar CMOS processing with surface micromachining to achieve the cross section shown in Fig. 10 [20], [25]. The technologies are combined in a modular fashion, in which the CMOS processing and surface micromachining are done in separate process modules, with no intermixing of CMOS or micromachining steps. This **M**odular **I**ntegration of **C**MOS and micro**S**tructures (MICS) process has the advantage in that it allows the use of nearly any CMOS process with a variety of surface micromachining processes.

In order to avoid problems with microstructure topography, which commonly includes step heights of 2–3 μm, the CMOS module is fabricated before the microstructure module. Although this solves topography problems, it introduces constraints on the CMOS. Specifically, the metallization and contacts for the electronics must be able to survive post-CMOS micromachining processing with temperatures up to 835 °C. Aluminum interconnect, the industry standard, cannot survive these temperatures. For this reason, tungsten with $TiSi_2$ contact barriers is used as interconnect for this process.

Unfortunately, the use of tungsten for circuit interconnect is not consistent with mainstream IC technologies, where aluminum interconnect predominates, and copper is on the rise. Given that IC manufacturers have already invested enormous resources into the development of multilevel aluminum or copper interconnect technologies, and further given the inferior resistivity of tungsten versus aluminum or copper,

the described tungsten-based post-CMOS process, although useful as a demonstration tool, is not likely to flourish in industry. Rather, other processes which intermix CMOS and micromachining fabrication steps [23] or which fabricate micromechanics before circuits (i.e., pre-circuit processes) [24] have become more prevalent. These processes, however, have their own associated limitations: mixed processes often require longer more expensive development periods for new product lines; while pre-circuit processes may place limitations on foundry-based fabrication schemes since circuit foundries may be sensitive to contamination from MEMS foundries. Thus, research aimed at achieving a truly modular merged circuit/microstructure technology is ongoing [26].

C. Oscillator Performance

As seen from Table II, resonator dc-bias voltages on the order of 35 V were required to obtain equivalent circuit R_x's in the range of hundreds of kΩ's for this early micromechanical resonator design. As will be seen, more recent μmechanical resonator designs used in bandpass filters allow much smaller operation voltages and can achieve much smaller values of motional resistance R_x (on the order of several ohms). Nevertheless, using V_P's in the range of 35 V and circuit supplies of 5 V, the oscillator of Fig. 5 was successfully operated and tested [20]. Oscillations were observed both electronically and visually under a microscope [20].

Currently (to the author's knowledge), commercial phase-noise measurement instrumentation is not available in the 16.5-kHz frequency range of this oscillator. Attempts to measure the $1/f^2$ phase noise using a custom-built measurement system were unsuccessful. However, at large offsets from the carrier frequency, the white-noise floor of the oscillator was clearly seen (using a spectrum analyzer) to have rather large magnitudes on the order of −70 dBc. This excessive white-noise floor arises from the limited power-handling capability of this particular μmechanical resonator [20] and underscores the importance of proper resonator design to achieve adequate short-term frequency stability. In other words, although the high Q of a μmechanical resonator can greatly reduce the close-to-carrier phase noise of a given oscillator, such an improvement is inconsequential if the power-handling capability of the resonator is unable to suppress white (of phase) noise to a comparable level, thus, the dynamic range of a given μmechanical resonator becomes of utmost importance in reference oscillator design. As will be shown in Section V, dynamic range improves with frequency for μmechanical resonators, thus, 10-MHz frequency references—which are more applicable to today's communications requirements—should not suffer from the same power-handling limitations. Research pursuant to realization of 10-MHz oscillators is currently underway.

D. Thermal Stability

Due to the extremely high-Q of the μmechanical resonator tank, the thermal stability of the overall oscillator is somewhat independent of the sustaining amplifier circuit and depends primarily on the temperature dependence of the μmechanical
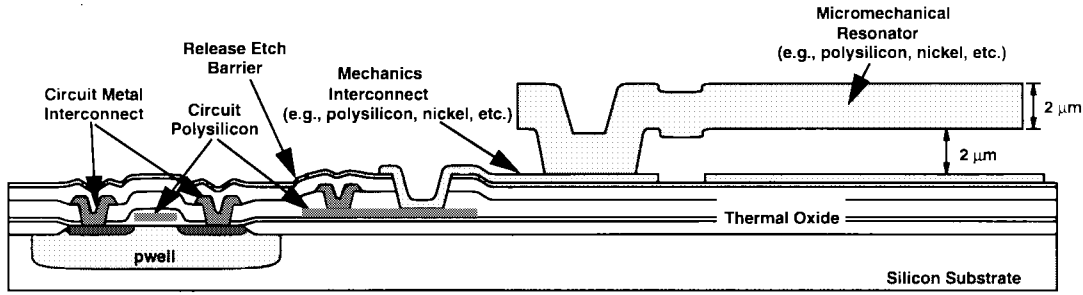
Fig. 10. Final cross section of the CMOS plus microstructures process used to realize the fully integrated oscillator of Fig. 5.
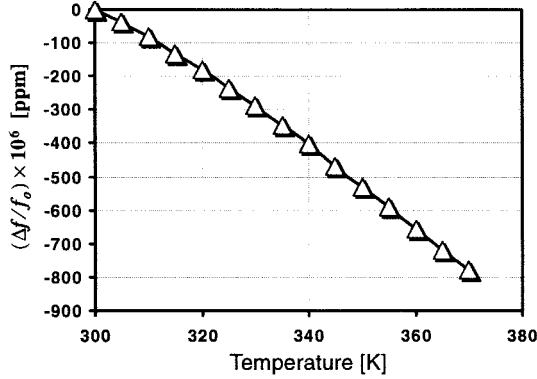

Fig. 11. Measured plot of fractional frequency change $\Delta f/f$ versus temperature for a folded-beam capacitive-comb transduced polysilicon μmechanical resonator. (Frequency measurements were made under small-amplitude linear conditions for this plot—i.e., $V_P = 20$ V and $v_i = 1$ mV.)

resonator. Fig. 11 shows a measured plot of fractional frequency change $\Delta f/f$ versus temperature for a folded-beam capacitive-comb transduced polysilicon μmechanical resonator fabricated using the surface micromachining process described above. From the slope of the curve, the temperature coefficient of the resonance frequency TC_{fr} for this device is -10 ppm/°C. Through manipulation of (1), the temperature coefficient of the Young's modulus TC_E may be expressed as

$$TC_E = 2TC_{fr} - TC_h. \tag{5}$$

Using the measured value of $TC_{fr} = -10$ ppm/°C, (5) yields $TC_E = -22.5$ ppm/°C. This value is considerably smaller than a previously reported number of -74.5 ppm/°C [27], and it is stated tentatively pending a more systematic study of other factors that can affect the TC_{fr}.

The measured TC_{fr} of -10 ppm/°C can be reduced further via on-chip compensation or on-chip oven-control techniques. Such integrated oven control has been demonstrated that reduced the TC_{fr} of a capacitive-comb transduced μresonator to -2 ppm/°C [14], at the cost of a more complex micromachining process.

IV. MICROMECHANICAL FILTERS

The measured spectrum of Fig. 6 represents the frequency characteristic for a second-order single-pole bandpass filter centered at 16.5 kHz. Although useful for some applications, such as pilot tone filtering in mobile phones, second-order filter characteristics are generally inadequate for the majority
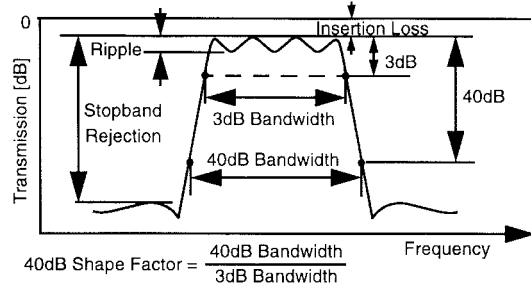

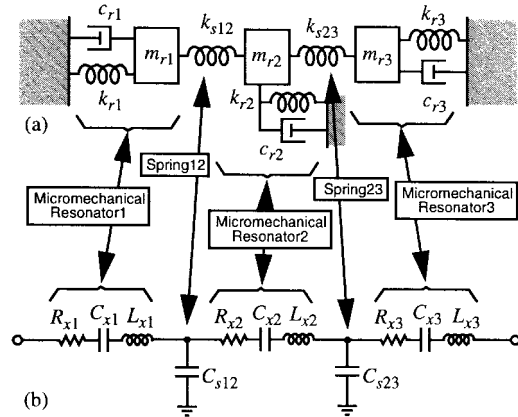Fig. 12. Parameters typically used for filter specification.

Fig. 13. (a) Equivalent lumped-parameter mechanical circuit for a mechanical filter. (b) Corresponding equivalent LCR network.

of communications applications. Rather, bandpass filters such as depicted generically in Fig. 12 are required, with flatter passbands, sharper rolloffs, and greater stopband rejections.

A. General Mechanical Filter Design Concepts

To achieve the characteristic of Fig. 12, a number of micromechanical resonators are linked together by soft coupling springs [28], as illustrated schematically in Fig. 13(a) using ideal mass-spring-damper elements. By linking resonators together using mechanical springs, a coupled resonator system is achieved that now exhibits several modes of vibration. As illustrated in Fig. 14 for the coupled three-resonator system of Fig. 13, the frequency of each vibration mode corresponds to a distinct peak in the force-to-displacement frequency characteristic, and to a distinct physical-mode shape of the coupled mechanical resonator system. In the lowest frequency mode, all resonators vibrate in phase; in the middle frequency
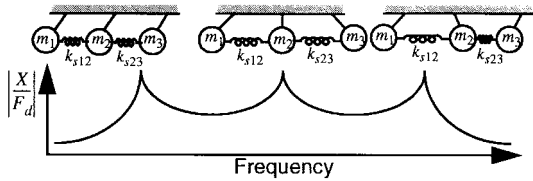
Fig. 14. Mode shapes of a three-resonator micromechanical filter and their corresponding frequency peaks.

mode, the center resonator ideally remains motionless, while the end resonators vibrate 180° out of phase; and, finally, in the highest frequency mode, each resonator is phase-shifted 180° from its adjacent neighbor. Without additional electronics, the complete mechanical filter exhibits the jagged passband seen in Fig. 14. As will be shown, termination resistors designed to lower the Q's of the input and output resonators by specific amounts are required to flatten the passband and achieve a more recognizable filter characteristic, such as in Fig. 12.

In practical implementations, because planar IC processes typically exhibit substantially better *matching* tolerances than *absolute*, the constituent resonators in μmechanical filters are normally designed to be identical, with identical spring dimensions and resonance frequencies. For such designs, the center frequency of the overall filter is equal to the resonance frequency f_o of the resonators, while the filter passband (i.e., the bandwidth) is determined by the spacings between the mode peaks.

The relative placement of the vibration peaks in the frequency characteristic—and, thus, the passband of the eventual filter—is determined primarily by the stiffnesses of the coupling springs (k_{sij}) and of the constituent resonators at the coupling locations (k_{rc}). In particular, for a filter with center frequency f_o and bandwidth B, these stiffnesses must satisfy

$$B = \left(\frac{f_o}{k_{ij}} \right) \left(\frac{k_{sij}}{k_{rc}} \right) \qquad (6)$$

where k_{ij} is a normalized coupling coefficient found in filter cookbooks [29]. Note from (6) that filter bandwidth is not dependent on the absolute values of resonator and coupling beam stiffness; rather, their ratio k_{sij}/k_{rc} dictates bandwidth. Thus, the procedure for designing a mechanical filter involves two main steps: first, design of a mechanical resonator with resonance frequency f_o and reasonable stiffness k_{rc}, and second, design of coupling springs with appropriate values of stiffness k_{sij} to achieve a desired bandwidth.

To take advantage of the maturity of *LC* ladder filter synthesis techniques, the enormous database governing *LC* ladder filter implementations [29], and the wide availability of electrical circuit simulators, realization of the μmechanical filter of Fig. 13(a) often also involves the design of an *LC* ladder version to fit the desired specification. The elements in the *LC* ladder design are then matched to lumped mechanical equivalents via electromechanical analogy, where inductance, capacitance, and resistance in the electrical domain equate to mass, compliance, and damping, respectively, in the mechanical domain. Fig. 13(b) explicitly depicts the equivalence between the filter's lumped mass–spring–damper circuit and its electrical equivalent circuit. As shown, for this particular

electromechanical analogy (the current analogy), each constituent resonator corresponds to a series *LCR* tank, while each (massless) coupling spring ideally corresponds to a shunt capacitor, with the whole coupled network corresponding to an *LC* ladder bandpass filter.

B. A Three-Resonator Medium-Frequency (MF) Micromechanical Filter

Fig. 15 shows the perspective-view schematic of a practical three-resonator micromechanical filter [16], [19]. As shown, this filter is comprised of three folded-beam μmechanical resonators mechanically coupled at their folding trusses by soft flexural-mode springs. The end resonators, which provide the filter inputs and outputs, feature capacitive comb transducers for enhanced linearity. In addition, these resonators, as well as the center resonator, are equipped with parallel-plate capacitive transducers capable of tuning their frequencies [16]. The entire μmechanical filter structure, including resonators and coupling springs, is constructed of doped (conductive) polycrystalline silicon, and is suspended 2 μm over a uniform doped-polysilicon ground plane that underlies the suspended structure at all points. This ground plane is required to prevent electrostatic pull-in of the structure into substrate, which can occur for structure-to-substrate voltage differences greater than 68 V.

To operate this filter, a dc-bias V_P is applied to the suspended movable structure, while differential ac signals v_i and $-v_i$ are applied through Q-controlling input resistors R_{Q11} and R_{Q12} to opposing ports of the input resonator, as shown in Fig. 15. The differential inputs applied to symmetrically opposing ports generate push–pull electrostatic forces on the input resonator, inducing mechanical vibration when the frequency of the input voltage comes within the passband of the mechanical filter. This vibrational energy is imparted to the center and output resonators via the coupling springs, causing them to vibrate as well. Vibration of the output resonator creates dc-biased time-varying capacitors between the resonator and respective port electrodes, which source output currents given by

$$i_{xin} = V_{\text{P}in} \frac{\partial C_{\text{in}}}{\partial x} \frac{\partial x}{\partial t} \qquad (7)$$

where x is displacement (defined in Fig. 15), C_{in} is the resonator-to-electrode capacitance at port n of resonator i, and $V_{\text{P}in}$ is the dc-bias voltage applied across C_{in}.

As shown in Fig. 15, the differential output currents i_{x31} and i_{x32} are directed through output Q-controlling resistors R_{Q31} and R_{Q32}, forming voltages across these resistors that are sensed by buffers A_1 and A_2, then directed to the differential-to-single-ended converter A_3. Note that these electronics are shown here only to suggest a convenient pick-off circuit for characterization of filters. They are not necessary in an actual transceiver implementation if the stage following the filter can be impedance matched to present effective R_{Q3n}'s in shunt with the outputs.

1) Quarter-Wavelength Coupling Beam Design: The equivalent mechanical circuit shown in Fig. 13(a) models an ideal case, where the springs coupling the resonators are massless. In
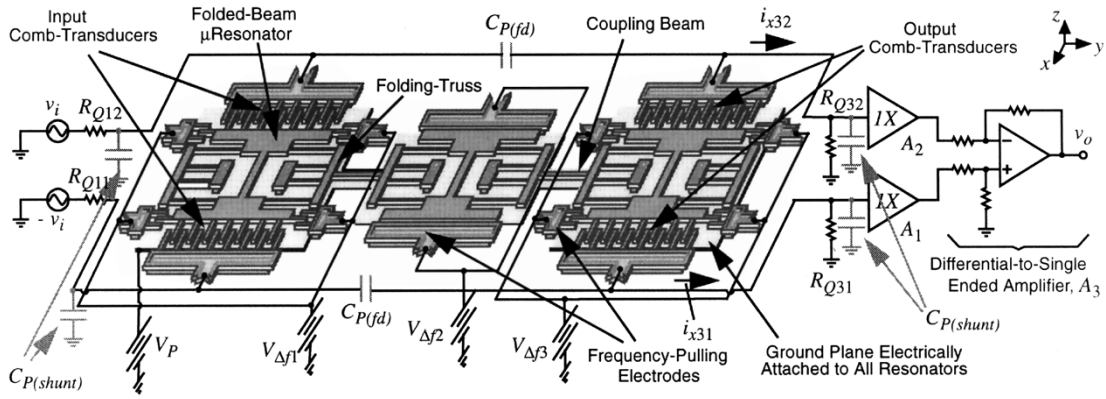
Fig. 15.   Schematic of a folded-beam three-resonator micromechanical filter with bias and excitation circuitry.
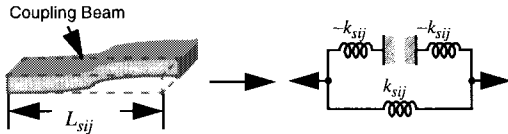

Fig. 16.   Equivalent mechanical circuit for a quarter-wavelength flexural-mode coupling beam.

Fig. 17.   Mechanical and (current analogy) electrical equivalent circuits for a quarter-wavelength coupled three-resonator micromechanical filter.

reality, the coupling springs have finite mass that, without special design precautions, can add to adjacent resonators, shifting their frequencies and causing distortion of the filter passband. As described in [16], in order to accommodate this finite coupling beam mass while retaining the use of identical resonators in a μmechanical filter, the dimensions of the coupling beams must correspond to an effective quarter-wavelength of the operation frequency. Specifically, for quarter-wavelength coupling, the length L_{sij}, width W_{sij}, and thickness h of a flexural-mode coupling beam must be chosen to simultaneously satisfy [16]

$$\cos\alpha\sinh\alpha + \sin\alpha\cosh\alpha = 0 \qquad (8)$$

$$k_{sij} = -\frac{EI_s\alpha^3(\sin\alpha + \sinh\alpha)}{L_{sij}^3(\cos\alpha\cosh\alpha - 1)} \qquad (9)$$

where $\alpha = L_{sij}(\rho A\omega_o^2/E/I_s)^{0.25}$, $I_s = hW_{sij}^3/12$, $A = W_{sij}h$, and k_{sij} satisfies (6).

The equivalent mechanical circuit for a quarter-wavelength coupling beam is effectively massless, consisting of a network of positive- and negative-valued springs with equal magnitudes, as shown in Fig. 16. Given this, the equivalent mechanical and simplified electrical (using the current analogy) circuits for a three-resonator micromechanical filter using quarter-wavelength coupling springs is shown in Fig. 17, where quarter-wavelength couplers in the electrical domain are seen to consist of capacitive T-networks. The electrical equivalent circuit in Fig. 17 is somewhat simplified in that it does not precisely model the multiport nature of the input and output resonators in a practical filter. For more precise modeling, multiport equivalent circuits, such as shown in Fig. 8, are required for the end resonators.
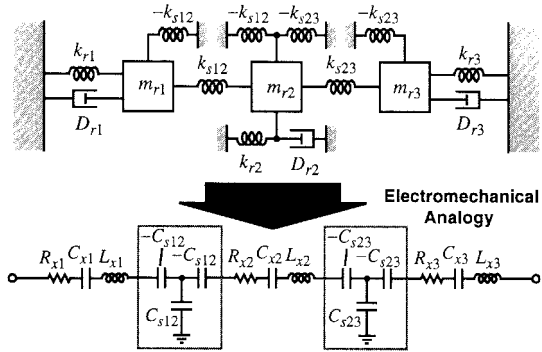
TABLE III
QUARTER-WAVELENGTH COUPLING BEAM REQUIREMENTS*

Percent BW [%]	W_{s12} [μm]	L_{s12} [μm]
0.01	0.06	16.8
0.1	0.29	36.2
0.67	1.02	68.2
1	1.33	77.9

*For a 455 kHz filter with k_{rc}=315 N/m and h=2μm.

For a given value of film thickness h, and a given needed value of coupling beam stiffness k_{sij}, (8) and (9) represent two equations in two unknowns, implying that only one set of values (W_{sij}, L_{sij}) can be used to implement a given stiffness k_{sij}. If the resonator stiffness is further constrained to be constant—as was the case for the design in [16]—a scenario could arise where the unique coupling beam width W_{sij} that satisfies both quarter-wavelength and filter bandwidth requirements is a submicrometer dimension. Table III illustrates this problem for the case of a 455-kHz polysilicon three-resonator filter coupled at the shuttle mass location (where the resonator stiffness is $k_{rc} = 315$ N/m), with $h = 2\,\mu$m. Here, submicrometer dimensions are shown to be necessary for percent bandwidths (B/f_o) lower than 0.67%.

2) Low-Velocity Coupling: To increase the required width of a quarter-wavelength coupling beam, the value of coupling beam stiffness k_{sij} corresponding to the needed filter bandwidth B must be increased. As indicated by
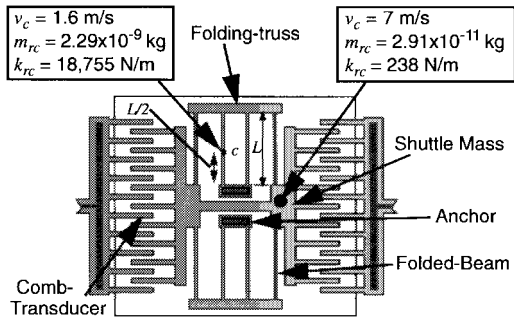
Fig. 18. Schematic of a classic folded-beam μresonator, indicating mechanical impedances at certain points.

Fig. 19. Schematic of a ratioed folded-beam μresonator for low-velocity coupling applications.

(6), for a given filter bandwidth, an increase in k_{sij} is allowable only when accompanied by an equal increase in resonator stiffness k_{rc}. Such an increase in k_{rc} must, in turn, be accompanied by a corresponding increase in resonator mass m_{rc} to maintain the desired filter center frequency. Thus, to maximize flexibility in attainable filter bandwidth, a convenient method for simultaneously scaling both resonator stiffness k_{rc} and mass m_{rc}, preferably without drastically changing overall resonator dimensions, is required.

One simple method for achieving this takes advantage of the fact that, in general, the effective dynamic stiffness and mass of a given resonator are strong functions of location on the resonator, as illustrated in Fig. 18, for a classic folded-beam μmechanical resonator. This is immediately apparent with the recognition that different locations on a vibrating resonator move with different velocities, and that the dynamic mass and stiffness of a given mechanical resonator are strong functions of velocity, given by [28]

$$m_{rc} = \frac{KE_{tot}}{(1/2)v_c^2} \qquad (10)$$

$$k_{rc} = \omega_o^2 m_{rc} \qquad (11)$$

where KE_{tot} is the total (peak) kinetic energy in the system integrated over all points, ω_o is radian resonance frequency, and v_c is the resonance velocity magnitude at location c on the resonator. As a result, the dynamic resonator mass and stiffness "seen" by a coupling beam is a strong function of the coupling location. Fundamental-mode folded-beam resonators coupled at their shuttle masses, where the velocity magnitude is maximum, present the smallest stiffness to the coupling beam. Conversely, fundamental-mode resonators coupled at locations closer to their anchors, where velocities are many times smaller, present very large dynamic stiffnesses to their respective coupling beams, allowing much smaller percent bandwidth filters for the same coupling beam stiffnesses.

To conveniently implement low-velocity coupling without substantial resonator design changes, and retaining coupling at resonator folding trusses, the folded-beam resonators used in Fig. 15 feature ratioed folded-beam lengths, as shown in Fig. 19 [19]. With this design, the resonance velocity magnitude of the folding truss can be varied according to
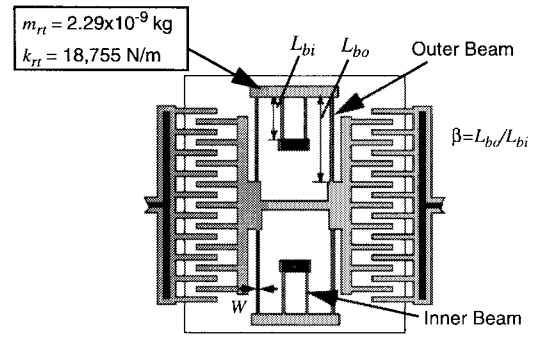
$$v_{rt} = \frac{\omega_o X_0}{1+\beta^3} \qquad (12)$$

where ω_o is the filter center frequency, X_o is the displacement magnitude at the shuttle mass, and β is the ratio of the outer beam length L_{bo} to inner beam length L_{bi}. Using (10) and (11), the effective dynamic stiffness k_{rt} and mass m_{rt} seen at the resonator folding trusses can be expressed as

$$k_{rt} = k_{rs}(1+\beta^3)^2 \qquad (13)$$

$$m_{rt} = m_{rs}(1+\beta^3)^2 \qquad (14)$$

where k_{rs} and m_{rs} are the effective dynamic stiffness and mass, respectively, at the resonator shuttle (maximum velocity point), given by

$$k_{rs} = \omega_o^2 m_{rs} \qquad (15)$$

$$m_{rs} = M_P + \frac{M_t}{(1+\beta^3)^2} + \frac{13}{35(1+\beta^3)^2}M_{bi}$$
$$+ \left[\frac{1}{(1+\beta^3)} + \frac{13\beta^6}{35(1+\beta^3)^2}\right]M_{bo} \qquad (16)$$

where

$$\omega_0 = \left[\frac{4Eh(W/L_{bi})^3}{(1+\beta^3)m_{rs}}\right]^{1/2}. \qquad (17)$$

and where E is the Young's modulus, M_P is the mass of the shuttle, M_t, M_{bi}, and M_{bo} are the total folding truss, inner beam, and outer beam masses, respectively; h is thickness, and other dimensions are defined in Fig. 19. It should be noted that (17) loses its accuracy for folded-beam lengths less than approximately 50 μm, when the stiffnesses of the folded beams become comparable to that of the folding trusses. Finite-element analysis should be used when (17) is insufficient.

Fig. 20 plots the dynamic stiffness (normalized against effective stiffness at the shuttle mass) at the folding truss versus β, showing a full six orders of magnitude variation in stiffness for β's from 1 to 10. For a 360-kHz filter with 2-μm-width coupling beams, the stiffness variation, shown in Fig. 20, corresponds to a range of percent bandwidths from 0.69% to 3×10^{-6}%.

3) Micromechanical Filter Termination: As mentioned previously, without the termination resistors R_{Qin}, shown in Fig. 15, the passband of the μmechanical filter would be as shown in Fig. 14, comprised of three peaks, with excessive ripple. To obtain the designed value of passband ripple, the Q of the end resonators must be controlled to specific values dictated by filter synthesis or by cookbook tables [29]. For the
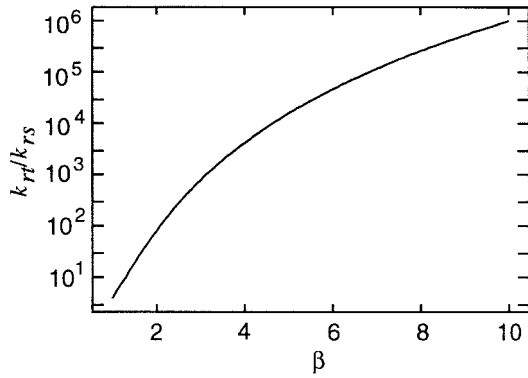
Fig. 20. Normalized effective stiffness at the folding-truss versus folded-beam ratio β.

Fig. 21. SEM's of a fabricated ratioed folded-beam micromechanical filter. (a) Full view. (b) Enlarged partial view.

design of Fig. 15, this is most easily done by placing resistors R_{Q1n} in series with each input and resistors R_{Q3n} in shunt with each output. The required resistor values are given by

$$R_{Qin} = \frac{1}{2}\left(\frac{Q_{\text{res}}}{q_i Q_{\text{fltr}}} - 1\right)R_{xin}, \qquad i = 1,3 \qquad (18)$$

where R_{xin} is defined in Fig. 8, Q_{res} is the initial uncontrolled quality factor of the constituent resonators, Q_{fltr} is the quality factor of the overall filter ($Q_{\text{fltr}} = (f_o/B)$), q_i is a normalized "q" value corresponding to the filter design in question (and easily found in filter cookbooks [29]), and n refers to a particular port of end resonator i.

The needed value of R_{Qin} is often set by impedance matching requirements to stages before and after the filter in question. Depending on whether the filter is used at the IF or RF, termination resistances in the range of 50 Ω–2 kΩ are often required. As will be seen, capacitive transduction provides for somewhat weak electromechanical coupling, thus, R_{Qin}'s tend to be larger than desired and design strategies that minimize their values are needed. From (18), R_{Qin} is best reduced by minimizing the value of R_{xin}, which, with reference to Fig. 8, is in turn best accomplished by maximizing $\partial C_{\text{in}}/\partial x$, assuming that V_P is restricted by power supply limitations. $\partial C_{\text{in}}/\partial x$ is best maximized by minimizing the gap spacing between resonator and electrode comb fingers and by increasing the total number of fingers.

4) MF Micromechanical Filter Performance: Wide-view and zoomed SEM's for a polysilicon surface-micromachined low velocity-coupled three-resonator μmechanical filter are presented in Fig. 21, with pointers to major components and key dimensions. The resonators in this filter are designed such that their folding truss resonance velocities are (7/32) the velocity at the shuttle ($\beta = 1.53$). Since the shuttle moves faster than any other location on the resonator during resonance, the shuttle location corresponds to the maximum velocity (v_{max}) point, and coupling at the folding trusses in this filter corresponds to $(7/32)v_{\text{max}}$ coupling. Design data for this filter, along with corresponding data for a $(1/2)v_{\text{max}}$ coupled filter ($\beta = 1$), are summarized in Table IV.

Fig. 22(a) and (b) compares transmission spectra for the $(1/2)v_{\text{max}}$ ($\beta = 1$) and $(7/32)v_{\text{max}}$ ($\beta = 1.53$) coupled μmechanical filters, respectively. As indicated in Table IV, even though the filter with $(1/2)v_{\text{max}}$ coupling utilizes more
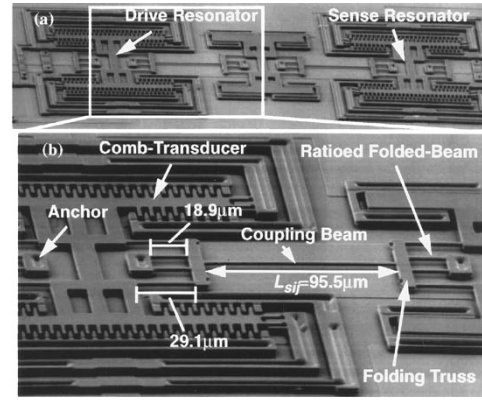
TABLE IV
MF MICROMECHANICAL FILTER DESIGN SUMMARY

Parameter	Value		Units
Coupling Velocity, v_c	$0.5v_{max}$	$0.22v_{max}$	—
Folded-Beam Ratio, β	1	1.53	—
Designed Bandwidth, B	1000	400	Hz
Measured Bandwidth, B	760	401	Hz
Percent Bandwidth, (B/f_o)	0.22	0.088	%
μRes. Folded-Beam Length, L_{bo}	24.8	29.1	μm
μRes. Folded-Beam Length, L_{bi}	24.8	18.9	μm
μRes. Folded-Beam Width, W_r	2	2	μm
Structural Layer Thickness, h	2	2	μm
Resonator Mass @ y_c, $m_{rc}=m_{rt}$	1×10^{-10}	8×10^{-10}	kg
Resonator Stiffness @ y_c, $k_{rc}=k_{rt}$	1,258	6,601	N/m
Comb-Finger Gap Spacing, d	1	1	μm
Comb-Finger Overlap, L_o	5	5	μm
Coupling Beam Length, $L_{s12}=L_{s23}$	74.6	95.5	μm
Coupling Beam Width, $W_{s12}=W_{s23}$	1.2	2	μm
Coupling Beam Stiffness, $k_{s12}=k_{s23}$	1.79	3.76	N/m
Young's Modulus, E	150	150	GPa
Density of Polysilicon, ρ	2,300	2,300	kg/m^3
Filter DC-Bias, V_P	170	160	V
Q-Control Resistors, $R_{Q1n}=R_{Q2n}$	474	364	kΩ

compliant 1 μm-wide coupling beams, this filter still exhibits a larger bandwidth (760 Hz, $Q_{\text{fltr}} = 459$) than its $(7/32)v_{\text{max}}$ coupled counterpart, which uses stiffer 2-μm-wide coupling beams, yet achieves a bandwidth of only 401 Hz ($Q_{\text{fltr}} = 813$). Furthermore, note from Table IV that the $(7/32)v_{\text{max}}$ coupled filter was able to closely match the target bandwidth (within 0.75%), unlike its $(1/2)v_{\text{max}}$ counterpart, which missed its target by 24.3%. This result can be attributed to the wider coupling beams of the lower velocity coupled filter, which are less susceptible to overetch-derived process variations than are the thinner beams of the higher velocity coupled one. Decreased process susceptibility is, thus, a major advantage afforded by low-velocity coupling strategies.

It is noteworthy to mention that the measured data in Fig. 22(a) and (b) illustrate not only the effectiveness of
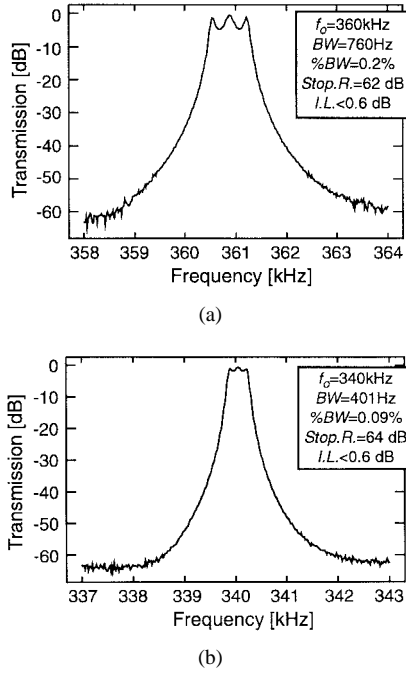
Fig. 22. Measured frequency spectra for low-velocity-coupled folded-beam MF filters. (a) Half-maximum velocity coupled. (b) 7/32-maximum velocity coupled.
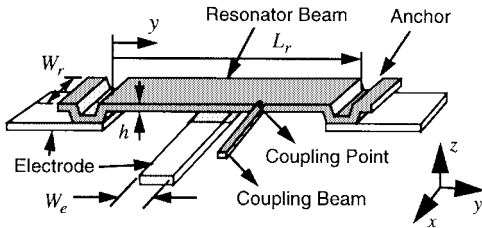

Fig. 23. Clamped–clamped beam μresonator.

low-velocity design techniques in achieving smaller percent bandwidths with improved accuracy, but also the impressive frequency response performance of μmechanical filters in general. In particular, Fig. 22(b) shows a filter response with a Q of 813, stopband rejection in excess of 64 dB, and an insertion loss of only 0.6 dB. Such performance rivals that of many macroscopic high-Q filters, including crystal filters, which are some of the best available.

C. A Two-Resonator HF Micromechanical Filter

As explained in [15], given the general expression for mechanical resonance frequency $\omega_o = (k_r/m_r)^{0.5}$, high frequency filters require resonators with much smaller mass. As a result, the folded-beam resonators used in the filter of Fig. 15 are inappropriate for HF or higher frequencies. Rather, clamped–clamped beam resonators, such as shown in Fig. 23, are more appropriate. Furthermore, as indicated in Table IV, some rather large voltages were required to achieve adequate electromechanical coupling via the comb-transducers shown in Fig. 15. To achieve more practical operation voltages and more reasonable R_Q's, more efficient transducers are needed.
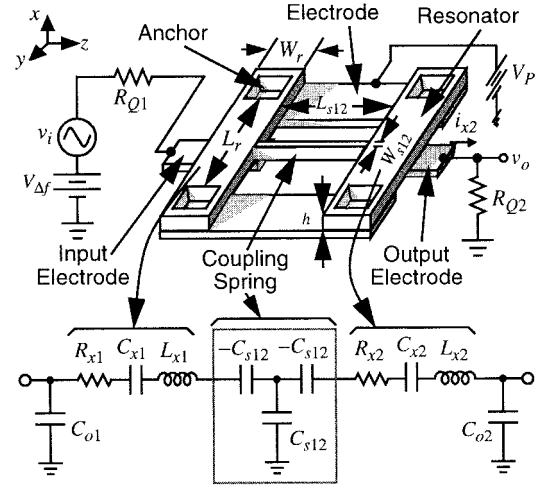

Fig. 24. Perspective view schematic of a two-resonator μmechanical filter, along with the preferred bias, excitation, and sensing circuitry, and the equivalent circuit for the filter.

1) HF Filter Structure and Operation: Fig. 24 presents the perspective view schematic of a two-resonator HF micromechanical filter, along with the preferred bias, excitation, and sensing circuitry. As shown, the filter consists of two μmechanical clamped–clamped beam resonators, coupled mechanically by a soft spring, all suspended 0.1–0.2 μm above the substrate. Conductive (polysilicon) strips underlie the central regions of each resonator and serve as capacitive transducer electrodes positioned to induce resonator vibration in a direction perpendicular to the substrate. The resonator-to-electrode gaps are determined by the thickness of a sacrificial oxide spacer during fabrication and can thus be made quite small (e.g., 0.1 μm or less) to maximize electromechanical coupling.

Under normal operation, the device is excited capacitively by a signal voltage applied to the input electrode. The output is taken at the other end of the structure, also via capacitive transduction. Upon application of an input with suitable frequency, the constituent resonators begin to vibrate in one or more flexural modes in a direction perpendicular to the substrate. For a properly designed mechanical filter, if the excitation voltage has a frequency within the passband, both resonators will vibrate. Vibration of the output resonator then couples to the output electrode, providing an output current i_{x2} given by an equation similar to (2), with x now representing displacement perpendicular to the substrate. The current i_{x2} is then directed to resistor R_{Q2}, which provides the proper termination impedance for the μmechanical filter.

2) HF Filter Design: As with the previous filter, if each μresonator is made identical, the filter center frequency is determined primarily by the frequency of the constituent resonators. For the parallel-plate capacitively transduced clamped–clamped beam resonators, shown in Fig. 24, the resonance frequency is given by

$$f_o = \frac{1}{2\pi}\sqrt{\frac{k_r}{m_r}} = 1.03\kappa\sqrt{\frac{E}{\rho}}\frac{h}{L_r^2}\left(1 - \left\langle\frac{k_e}{k_m}\right\rangle\right)^{1/2} \quad (19)$$

where

$$\left\langle \frac{k_e}{k_m} \right\rangle = \int_{0.5(L_r - W_e)}^{0.5(L_r + W_e)} \frac{V_P^2 \varepsilon_o W_r \, dy}{k_m(y)\big(d(y)\big)^3} \qquad (20)$$

and where: 1) m_r and k_r are the effective mass and stiffness at a given location on the resonator; 2) E and ρ are the Young's modulus and density of the structural material, respectively; 3) h, L_r, and W_r are specified in Fig. 24; 4) it has been assumed that $W_e = (1/2)L_r$; 5) ε_o is the permittivity in vacuum; 6) the function $\langle k_e/k_m \rangle$ models the effect of an electrical spring stiffness k_e that arises when a bias voltage is applied across the electrode-to-resonator gap, and that subtracts from the mechanical stiffness $k_m(y)$; 7) $d(y)$ is the electrode-to-resonator gap spacing as a function of location, which changes due to beam bending under a static V_P load; and 8) κ is a scaling factor that models the effects of surface topography. For the μresonators of this work, κ is dominated by anchor step-up and finite elasticity effects [30], [31], which are predictable using finite-element analysis (FEA). In practice, assuming a set value for V_P, designing for a specific frequency amounts to setting geometric dimensions L_r, W_r, and W_e via computer-aided design (CAD) layout since all other variables are determined at the outset by fabrication technology.

Note from (19) and (20) that the resonance frequency f_o of this device is tunable via adjustment of the dc-bias voltage V_P, and this can be used advantageously to implement filters with tunable center frequencies or to correct for passband distortion caused by finite planar fabrication tolerances. The dc-bias dependence of f_o arises from a V_P-dependent electrical stiffness k_e generated by the nonlinear dependence of electrode-to-resonator gap capacitance $C(x)$ on displacement x [12], [32]. This electrical stiffness effectively subtracts from the resonator mechanical stiffness $k_m(y)$ at each location y above the electrode, lowering the overall spring stiffness at that location to $k_r(y) = k_m(y) - dk_e(y)$, and contributing to the overall frequency shift (which is obtained by integrating over the electrode width). As seen from (20), the degree of frequency shift is approximately proportional to (V_P^2/d^3).

The design procedure for HF micromechanical filters is virtually identical to that for the previous MF filters, differing only in the specific equations used [33]. Electromechanical analogies are again utilized to design this filter, the bandwidth is again dictated by (6), and again, quarter-wavelength coupling beams and low-velocity coupling are utilized to achieve small-percent bandwidths accurately. For clamped–clamped beam resonators, low velocity coupling is very easily achieved by merely moving the coupling location away from the center of the beam, as shown in Fig. 23. Using a procedure similar to that used to obtain (13) and (14), expressions for dynamic stiffness and mass as a function of distance y from an anchor are derived to be

$$k_r(y) = \omega_o^2 m_r(y) \qquad (21)$$

$$m_r(y) = \frac{\rho W_r h \int_0^{L_r} \big[X(y')\big]^2 \, dy'}{\big[X(y)\big]^2} \qquad (22)$$
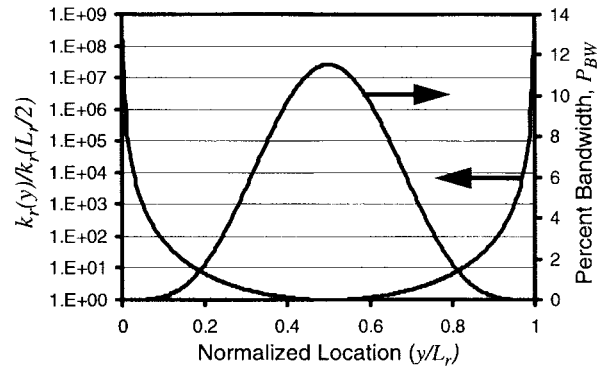

Fig. 25. Normalized effective μresonator stiffness versus normalized location on the resonator beam. Percent bandwidths are also given for an 8.71-MHz filter using 40.8-μm-long beams and a quarter-wavelength coupling beam with $k_{s12} = 92.5$ N/m.
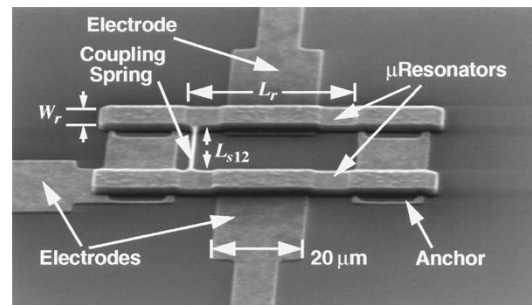

Fig. 26. SEM of a spring-coupled HF bandpass μmechanical filter.

where

$$X(y) = (\cos ky - \cosh ky) - \sigma_n (\sin ky - \sinh ky) \qquad (23)$$

and where $k = 4.73/L_r$ and $\sigma_n = 0.9825$ for the fundamental mode, and dimensions are indicated in Fig. 23.

Fig. 25 plots stiffness (normalized against the stiffness at the center of the resonator beam) versus normalized distance from an anchor for an ideal clamped–clamped beam resonator, indicating a two order of magnitude variation in stiffness for coupling locations $L_r/10$ to $L_r/2$ distant from the anchor. For an 8.71-MHz filter using 40.8-μm-long beams and a quarter-wavelength coupling beam with $k_{s12} = 92.5$ N/m, this corresponds to a range of percent bandwidths from 0.16% to 11.5%. It should be noted that although the use of maximum velocity coupling can separate the mode peaks of this μmechanical filter by 11.5% of the center frequency, the actual realizable bandwidth in a practical design will most likely be dictated by termination resistance requirements—i.e., by electromechanical coupling.

3) HF Micromechanical Filter Performance: The SEM for an 8.71-MHz two-resonator low-velocity coupled micromechanical filter constructed of phosphorous-doped polysilicon is shown in Fig. 26. Design details for this filter are summarized in Table V, along with operation voltages and Q-controlling resistor values. Note from the table that due to the use of small electrode-to-resonator gap spacings, a dc-bias voltage V_P much smaller than required for the previous comb-driven filter can now be used, and Q-controlling termination resistors are now on the order of 12.2 kΩ. With even smaller

TABLE V
HF μmechanical FILTER DATA

Parameter	Value	Units
μResonator Beam Length, L_r	40.8	μm
μResonator Beam Width, W_r	8	μm
Structural Layer Thickness, h	1.9	μm
μResonator Effective Mass, m_{re}	5.66×10^{-13}	kg
μResonator Spring Constant, k_{re}	1,362	N/m
Electrode-to-Resonator Overlap	160	μm^2
Electrode-to-Resonator Gap, d	0.198	μm
Freq. Pulling Factor, $<k_e/k_m>$	0.124	—
Coupling Beam Length, L_{s12}	20.35	μm
Coupling Beam Width, W_{s12}	0.75	μm
P_{BW} at l_c=4.48 μm (calculated)*	0.23%	—
P_{BW} at l_c=4.48 μm (measured)*	0.23%	—
P_{BW} at l_c=10 μm (calculated)*	3.2%	—
P_{BW} at l_c=10 μm (measured)*	2.5%	—
Dc-bias Voltage, V_P	35	V
Termin. Resistors (for l_c=10 μm), R_{Qi}	12.2	kΩ

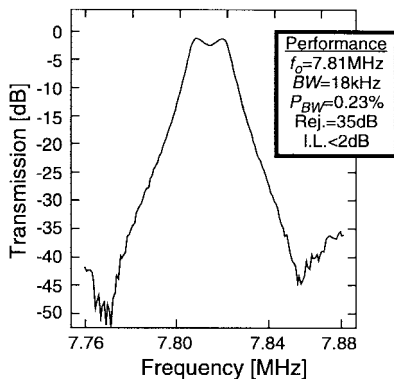* P_{BW} = percent bandwidth. l_c is the effective distance from the anchor to the coupling location.

Fig. 27. Measured transmission spectrum for an HF two-resonator micromechanical filter, such as shown in Fig. 26.

Fig. 28. Measured transconductance spectra for: (a) $POCl_3$-doped resonator and (b) implant-doped version, both after furnace annealing.

gaps, lower values of V_P and R_Q are expected. For example, for the filter of Table V, an electrode-to-resonator gap spacing of 300 Å would allow the use of a 3-V dc-bias with 1.1-kΩ termination resistors.

The measured transmission spectrum for a $(0.14)v_{\mathrm{max}}$-coupled filter (effective coupling distance from the anchor $l_c = 4.48 \mu$m; actual coupling distance $l_c = 4.08 \mu$m) is presented in Fig. 27. As shown, a percent bandwidth of 0.23% was achieved with an associated insertion loss of less than 2 dB, and a stopband rejection exceeding 35 dB. Again, these are impressive figures for a two-resonator bandpass filter, clearly indicative of the use of high-Q resonators.

V. FREQUENCY RANGE OF APPLICABILITY

If micromechanical resonator devices are to realize the RF channel-select receiver architecture of Fig. 4 for military and commercial handset applications, then the HF frequencies shown above must be extended to the high VHF and UHF
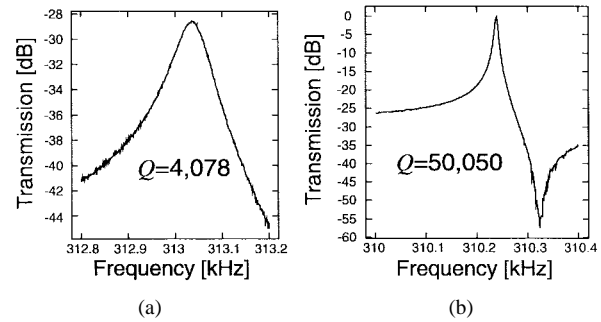
ranges. Thus, the ultimate frequency range of the described micromechanical resonators is of great interest and is currently a topic under intense study. From a purely geometric standpoint, the frequency range of micromechanical resonators can extend well into the gigahertz range. For example, the dimensions of a clamped–clamped beam resonator required to attain a frequency of 1 GHz are (referring to Fig. 1) approximately $L \approx 4 \mu$m, $W = 2 \mu$m, and $h = 2 \mu$m, where FEA should be used to account for width and anchoring effects. This frequency can also be attained by longer beams vibrating in higher modes. Thus, according to analytical and finite-element prediction, frequencies into the gigahertz range are geometrically possible.

Geometry, however, is only one of many important considerations. The applicable frequency range of micromechanical resonators will also be a function of several other factors, including: 1) Q factor, which may change with frequency for a given material, depending upon frequency-dependent energy loss mechanisms [34]; 2) series motional resistance R_x (cf. Fig. 24), which must be minimized to allow impedance matching with other transceiver components and to suppress input-referred noise and alleviate filter passband distortion due to parasitics [15], [16], [20], [33]; 3) absolute and matching tolerances of resonance frequencies, which will both be functions of the fabrication technology and of frequency trimming or tuning strategies [35]; and 4) stability of the resonance frequency against temperature variations, mass loading, aging, and other environmental phenomena. Each of the above phenomena are currently under study. In particular, assuming adequate vacuum can be achieved, the ultimate Q factor will be strongly dependent upon the material type, and even the manufacturing process. For example, surface roughness or surface damage during fabrication may play a role in limiting Q factor. In fact, preliminary results comparing the Q factor achievable in diffusion-doped polysilicon structures (which exhibit substantial pitting of the poly surface) versus implant-doped ones, indicate that the latter exhibit almost an order of magnitude higher Q at frequencies near 10 MHz. Fig. 28 presents measured transconductance spectra for two comb-driven folded-beam micromechanical resonators fabricated in the same polycrystalline material, but doped differently—one $POCl_3$-doped, the other phosphorous implant-doped using the process sequences summarized in Table VI [35]. The difference in Q is very intriguing, and

TABLE VI
DOPING RECIPES

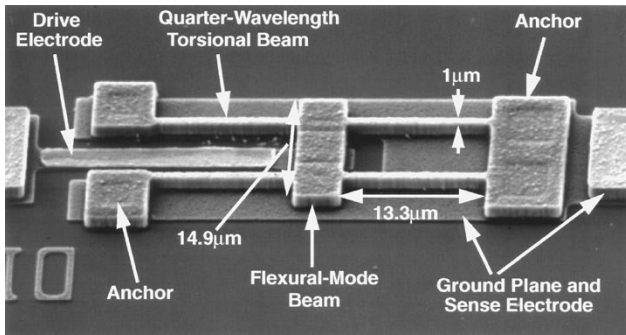| POCl$_3$	Implant
(i) Deposit 2 μm LPCVD fine-grained polysilicon @ 588°C	(i) Deposit 1 μm LPCVD fine-grained polysilicon @ 588°C
(ii) Dope 2.5 hrs. @ 950°C in POCl$_3$ gas	(ii) Implant phosphorous: Dose=10^{16} cm^{-2}, Energy=90 keV
(iii) Anneal for 1 hr. @ 1100°C in N$_2$ ambient	(iii) Deposit 1 μm LPCVD fine-grained polysilicon @ 588°C
	(iv) Anneal for 1 hr. @ 1100°C in N$_2$ ambient

Fig. 29. SEM of free–free beam virtually levitated micromechanical resonator with relevant dimensions for $f_o = 71$ MHz.

Fig. 30. Frequency characteristic for a fabricated 92.25-MHz free–free beam micromechanical resonator.

is consistent with a surface roughness-dependent dissipation mechanism.

From a design perspective, one Q-limiting loss mechanism that becomes more important with increasing frequency is loss to the substrate through anchors. The frequency dependence of this mechanism arises because the stiffness of a given resonator beam generally increases with resonance frequency, giving rise to larger forces exerted by the beam on its anchors during vibration. As a consequence, more energy per cycle is radiated into the substrate via the anchors. Antisymmetric resonance designs, such as balanced tuning forks, could prove effective in alleviating this source of energy loss.

Alternatively, anchor loss mechanisms can be greatly alleviated by using "anchorless" resonator designs, such as shown in Fig. 29. This recently demonstrated device utilizes a free-free beam (i.e., xylophone) resonator suspended by four torsional supports attached at flexural node points. By choosing support dimensions corresponding to a quarter-wavelength of the free–free beam's resonance frequency, the impedance presented to the beam by the supports can be effectively nulled out, leaving the beam virtually levitated and free to vibrate as if it had no supports [36]. Fig. 30 presents the frequency characteristic for a 92.25-MHz version of this μmechanical resonator, showing a Q of nearly 8000—still plenty for channel-select RF applications. (Note that the excessive loss in the spectrum of Fig. 30 is an artifact of improper impedance matching between the resonator output and the measurement apparatus. In addition, this resonator used a conservative electrode-to-resonator gap spacing of $d \sim 2000$ Å, so a rather large V_P was needed to provide a sufficient output level.)
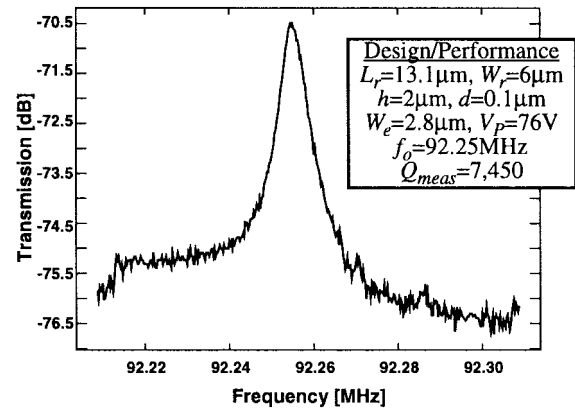
A. Electromechanical Coupling

In addition to possible Q limitations, the practical frequency range of micromechanical resonators is limited by electromechanical coupling, which is largest when the series motional resistance R_x is smallest. R_x, indicated in Fig. 8, is given by [20]

$$R_x = \frac{\sqrt{k_{\mathrm{re}} m_{\mathrm{re}}}}{Q V_P^2 (\partial C / \partial x)^2} \tag{24}$$

where k_{re} and m_{re} are the average lumped stiffness and mass of the resonator at the electrode center location. Given that a frequency increase on this micro-scale entails an increase in k_{re} with only a slight decrease in mass m_{re}, (24) suggests that R_x increases gradually with frequency. For a given frequency, R_x may be reduced by increasing the dc-bias V_P or the $\partial C / \partial x$ term. The value to which V_P may be raised is limited by the available supply voltage or by the maximum voltage obtainable through charge pumping. For the HF filter described above, the $\partial C / \partial x$ term is proportional to the electrode-to-resonator overlap area and inversely proportional to the square of the electrode-to-resonator gap spacing. The overlap area is limited by width effects on the resonance frequency, while the gap spacing is limited by technology. In particular, the gap spacing is defined by an oxide spacer thickness and, thus, can be made very small, on the order of tens to hundreds of angstroms. For this reason, the minimum gap spacing is likely not determined by process limitations, but rather by dynamic range considerations.

B. Dynamic Range

The dynamic range in the passband of a μmechanical filter can be determined through consideration of nonlinearity in its electromechanical transducers and noise produced by its termination resistors. For the purposes of deriving an expression for filter dynamic range in the passband, Fig. 31 presents the equivalent circuit for an n-resonator filter for input frequencies within the passband.

Dynamic range in the filter passband is defined by the ratio of the maximum input power $v_{i\max}^2$ (determined by nonlinearity) to the minimum detectable signal $\overline{v_n^2}$ (determined
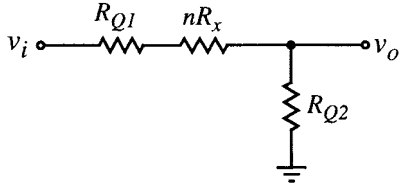
Fig. 31. Equivalent circuit for an n-resonator micromechanical filter for input frequencies within the passband.

by input-referred noise), i.e.,

$$DR = \frac{v_{i\,\mathrm{max}}^2}{v_n^2}. \tag{25}$$

The total input-referred noise power in this passive system is comprised primarily of thermal noise from the termination resistor R_{Q1}, plus small contributions from the resonator R_x's, which actually represent Brownian motion noise of the constituent resonators. The output termination resistor R_{Q2} is normally realized by the input to the following stage (e.g., an amplifier), which often exhibits less noise than a physical resistor with value R_{Q2}. For this reason, along with the conviction that noise from the following stage should not be associated with the μresonator, R_{Q2} will be considered noiseless in this analysis. An expression for the total input-referred noise power for a terminated n-resonator filter is then given by

$$\overline{v_n^2} = 4k_BT(R_Q + nR_x)\Delta f \approx 4k_BT(R_Q)\Delta f \tag{26}$$

where k_B is Boltzmann's constant, T is temperature, it has been assumed that $R_{Q1} = R_{Q2} = R_Q$, and the last equation holds for filters with low insertion loss (i.e., $R_Q \gg R_x$).

The maximum input voltage $v_{i\,\mathrm{max}}$ is determined by the maximum allowable displacement that maintains adequate transducer linearity or resonator stiffness linearity. If displacements x are assumed small enough that stiffness nonlinearity is not an issue, then the maximum allowable input voltage with frequency in the filter passband is given

$$v_{i\,\mathrm{max}} = \frac{2k_{\mathrm{re}}x_{\mathrm{max}}}{q_iQ_{\mathrm{fltr}}V_P(\partial C/\partial x)} \tag{27}$$

where k_{re} is the average resonator stiffness lumped at the center location of the input electrode, and x_{max} is the maximum allowable displacement magnitude at the electrode center location determined by nonlinear distortion. Note that for the case of flexural-mode beam μresonators using parallel-plate capacitive transducers, such as in Figs. 23 and 29, k_{re} is not given directly by (21), but rather must be obtained by integrating (21) over the electrode width to account for the location dependence of $k_r(y)$.

Inserting (26) and the rms value of (27) into (25), an approximate expression for the dynamic range in the passband of the filter in Fig. 31 is

$$DR = 10\log\left[\frac{\pi}{q_i}\frac{k_{\mathrm{re}}x_{\mathrm{max}}^2}{k_BT}\right] \quad \text{in dB.} \tag{28}$$

For the case where clamped–clamped beam, parallel-plate capacitively transduced μmechanical resonators are used in

the filter, (28) reduces to

$$DR = 10\log\left[\frac{\pi}{q_i}\frac{k_{\mathrm{re}}a^2d^2}{k_BT}\right] \quad \text{in dB} \tag{29}$$

where d is the electrode-to-resonator gap spacing at both input and output transducers, and a is a constant determined by the magnitude of acceptable IM_3 distortion [37]. Note that DR increases with both resonator stiffness k_{re} and gap spacing d. Unfortunately, R_x (hence, R_Q) also increases with increases in both these parameters, implying that dynamic range must be sacrificed in order to reduce R_Q to needed values—typically in the range of 50 Ω–2 kΩ for impedance-matching purposes in most transceivers.

To investigate the effect of frequency scaling on the dynamic range of a given micromechanical filter, we first propose a scaling strategy in which the frequency of a given filter is increased by increasing k_{re} while scaling d to maintain a constant R_{Qi}, with all other parameters held constant (including mass m_{re}). Note that for the HF micromechanical filter shown in Fig. 26, a frequency increase via the mere reduction of beam length L_r follows this scaling rule to first order since mass m_{re} decreases very slowly when L_r scales, while stiffness k_{re} increases rapidly to account for the majority of the frequency increase.

In order to satisfy the constant R_{Qi} requirement, an expression is needed for the termination resistance of a clamped–clamped beam micromechanical resonator. Using (18) and (24), and recognizing that

$$\frac{\partial C}{\partial x} \sim \frac{\varepsilon_o W_r W_e}{d^2} \tag{30}$$

for parallel-plate capacitively driven devices, R_{Qi} for the HF micromechanical filter of Fig. 26 takes on the form

$$R_{Qi} \approx \frac{P_{BW}}{q_i}\frac{\sqrt{k_{\mathrm{re}}m_{\mathrm{re}}}}{\varepsilon_o W_r W_e}\frac{d^4}{V_P^2}. \tag{31}$$

Using (31) with (19) and (29), the relevant dependencies under a given frequency scaling can be comparatively written out as

$$f_o \sim \sqrt{k_{\mathrm{re}}}$$
$$f_o \sim \frac{1}{L_r^2} \tag{32}$$
$$W_e = \frac{L_r}{2} \sim L_r \tag{33}$$
$$DR \sim d\sqrt{k_{\mathrm{re}}} \tag{34}$$
$$R_{Qi} \sim \frac{d^4\sqrt{k_{\mathrm{re}}}}{W_e} \tag{35}$$

Using these equations, if f_o scales by N, also scales by N, L_r, and W_e scale by $N^{-1/2}$, and d must scale by $N^{-3/8}$ to maintain a constant R_{Qi}. Equation (34) then predicts that DR scales by $N^{5/8}$. Thus, under the described "nearly constant mass/constant R_{Qi}" scaling rule, dynamic range increases with increasing frequency—a fortuitous result given present goals to extend resonator frequencies toward UHF.

Although encouraging, the above result may not be applicable to all cases since it not only neglects mass changes with frequency, but also neglects possible dc-bias V_P limitations

incurred when d becomes extremely small (and pull-in must be avoided). Specifically, there will most likely be a point at which V_P must also be scaled as d decreases in order to prevent pull-in of the resonator to its electrode, and this adds an additional component to (35) that will slow the DR increase with f_o. For this reason, alternative methods for dynamic range enhancement, such as the use of more linear and more efficient transducers, are currently under investigation.

VI. CONCLUSIONS

High-Q filters and oscillators utilizing micromechanical vibrating resonator tanks have been demonstrated with frequencies from LF to VHF, and requiring areas of less than 0.005 mm^2 per device on average. The tiny size, high selectivity, switchability, and zero dc power consumption of these devices together may make possible transceiver architectures that harness the selectivity (or Q) versus power tradeoffs so often seen in communication subsystem design. In particular, when used in transceiver architectures that emphasize selectivity over complexity, such passive micromechanical signal processors can potentially enable substantial power savings by relaxing the power requirements of the surrounding transistor-based transceiver stages (e.g., LNA's, mixers, A/D converters).

From a purely geometrical standpoint, the described IC-compatible mechanical resonators should be able to achieve vibrational frequencies well into the gigahertz range. However, considerations other than geometry, such as frequency-dependent loss mechanisms, electromechanical coupling, and matching tolerances, all of which affect the ultimate performance of the described oscillators and filters, will most likely dictate the ultimate frequency range of this technology. For the case of filters, dynamic range and the need for small termination impedances are found to be competing attributes in some designs. The tradeoffs, however, can be made much less severe with proper design techniques at higher frequencies.

ACKNOWLEDGMENT

The author gratefully acknowledges substantial contributions from former and present graduate students, in particular K. Wang, A.-C. Wong, and F. Bannon III, who are responsible for the filter results.

REFERENCES

[1] A. M. Niknejad and R. G. Meyer, "Analysis, design, and optimization of spiral inductors and transformers for Si RF IC's," *IEEE J. Solid-State Circuits*, vol. 33, pp. 1470–1480, Oct. 1998.
[2] C. P. Yue and S. S. Wong, "On-chip spiral inductors with patterned ground shields for Si-based RF IC's," *IEEE J. Solid-State Circuits*, vol. 33, pp. 743–751, May 1998.
[3] J. Craninckx and M. S. J. Steyaert, "A 1.8-GHz low-phase-noise CMOS VCO using optimized hollow spiral inductors," *IEEE J. Solid-State Circuits*, vol. 32, pp. 736–744, May 1997.
[4] S. V. Krishnaswamy, J. Rosenbaum, S. Horwitz, C. Yale, and R. A. Moore, "Compact FBAR filters offer low-loss performance," *Microwaves RF*, vol. 30, no. 9, pp. 127–136, Sept. 1991.
[5] R. Ruby and P. Merchant, "Micromachined thin film bulk acoustic resonators," in *Proc. IEEE Int. Frequency Control Symp.*, Boston, MA, June 1–3, 1994, pp. 135–138.
[6] A. A. Abidi, "Direct-conversion radio transceivers for digital communications," *IEEE J. Solid-State Circuits*, vol. 30, pp. 1399–1410, Dec. 1995.
[7] D. H. Shen, C.-M. Hwang, B. B. Lusignan, and B. A. Wooley, "A 900-MHz RF front-end with integrated discrete-time filtering," *IEEE J. Solid-State Circuits*, vol. 31, pp. 1945–1954, Dec. 1996.
[8] J. C. Rudell, J.-J. Ou, T. B. Cho, G. Chien, F. Brianti, J. A. Weldon, and P. R. Gray, "A 1.9-GHz wide-band IF double conversion CMOS receiver for cordless telephone applications," *IEEE J. Solid-State Circuits*, vol. 32, pp. 2071–2088, Dec. 1997.
[9] C. T.-C. Nguyen, "Frequency-selective MEMS for miniaturized communication devices," in *Proc. IEEE Aerospace Conf.*, Snowmass, CO, Mar. 21–28, 1998, pp. 445-460.
[10] C. T.-C. Nguyen, L. P. B. Katehi, and G. M. Rebeiz, "Micromachined devices for wireless communications," *Proc. IEEE*, vol. 86, pp. 1756–1768, Aug. 1998.
[11] W. C. Tang, T.-C. H. Nguyen, and R. T. Howe, "Laterally driven polysilicon resonant microstructures," *Sens. Actuators*, vol. 20, pp. 25–32, 1989.
[12] R. T. Howe and R. S. Muller, "Resonant microbridge vapor sensor," *IEEE Trans. Electron Devices*, vol. ED-33, pp. 499–506, Apr. 1986.
[13] C. T.-C. Nguyen and R. T. Howe, "Quality factor control for micromechanical resonators," in *IEEE Int. Electron Devices Meeting Tech. Dig.*, San Francisco, CA, Dec. 14–16, 1992, pp. 505–508
[14] ——, "Microresonator frequency control and stabilization using an integrated micro oven," in *7th Int. Solid-State Sensors Actuators Conf. Tech. Dig.*, Yokohama, Japan, June 7–10, 1993, pp. 1040–1043.
[15] F. D. Bannon III and C. T.-C. Nguyen, "High frequency microelectromechanical IF filters," *IEEE Electron Devices Meeting Tech. Dig.*, 1 San Francisco, CA, Dec. 8–11, 1996, pp. 773–776.
[16] K. Wang and C. T.-C. Nguyen, "High-order micromechanical electronic filters," in *Proc., IEEE Int. MEMS Workshop*, Nagoya, Japan, Jan. 26–30, 1997, pp. 25–30.
[17] J. R. Clark, A.-C. Wong, and C. T.-C. Nguyen, "Parallel-resonator HF micromechanical bandpass filters," in *Int. Solid-State Sensors Actuators Conf. Tech. Dig.*, Chicago, IL, June 16–19, 1997, pp. 1161–1164.
[18] C. T.-C. Nguyen, A.-C. Wong, and H. Ding, "Tunable, switchable, high-Q VHF microelectromechanical bandpass filters," in *IEEE Int. Solid-State Circuits Conf. Tech. Dig.*, San Francisco, CA, Feb. 15–17, 1999, pp. 78–79, 448.
[19] K. Wang, J. R. Clark, and C. T.-C. Nguyen, "Q-enhancement of micromechanical filters via low-velocity spring coupling," in *Proc. IEEE Int. Ultrason. Symp.*, Toronto, Ont., Canada, Oct. 5–8, 1997.
[20] C. T.-C. Nguyen and R. T. Howe, "An integrated CMOS micromechanical resonator high-Q oscillator," *IEEE J. Solid-State Circuits*, vol. 34, pp. 440–445, Apr. 1999.
[21] ——, "Design and performance of monolithic CMOS micromechanical resonator oscillators," in *Proc., IEEE Int. Frequency Control Symp. Dig.*, Boston, MA, May 31–June 3, 1994, pp. 127–134.
[22] T. A. Roessig, R. T. Howe, and A. P. Pisano, "Surface-micromachined 1 MHz oscillator with low-noise Pierce configuration," in *Solid-State Sensor Actuator Workshop Tech. Dig.*, Hilton Head, SC, June 8–11, 1998, pp. 328–332.
[23] T. A. Core, W. K. Tsang, S. J. Sherman, "Fabrication technology for an integrated surface-micromachined sensor," *Solid State Technol.*, vol. 36, no., 10, pp. 39–47, Oct. 1993.
[24] R. D. Nasby, J. J. Sniegowski, J. H. Smith, S. Montague, C. C. Barron, W. P. Eaton, P. J. McWhorter, D. L. Hetherington, C. A. Apblett, and J. G. Fleming, "Application of chemical-mechanical polishing to planarization of surface-micromachined devices," in *Solid-State Sensor Actuator Workshop Tech. Dig.*, Hilton Head, SC, June 3–6, 1996, pp. 48–53.
[25] J. M. Bustillo, G. K. Fedder, C. T.-C. Nguyen, and R. T. Howe, "Process technology for the modular integration of CMOS and polysilicon microstructures," *Microsyst. Technol.*, vol. 1, pp. 30–41, 1994.
[26] A. E. Franke, D. Bilic, D. T. Chang, P. T. Jones, T.-J. King, R. T. Howe, and G. C. Johnson, "Post-CMOS integration of germanium microstructures," in *12th Int. IEEE MEMS Conf. Tech. Dig.*, Orlando, FL, Jan. 17–21, 1999, pp. 630–637.
[27] H. Guckel *et al.*, "The mechanical properties of fine-grained polysilicon: The repeatability issue," in *IEEE Solid-State Sensor Actuator Workshop Tech. Dig.*, Hilton Head, SC, June 1988, pp. 96–99.
[28] R. A. Johnson, *Mechanical Filters in Electronics*. New York: Wiley, 1983.
[29] A. I. Zverev, *Handbook of Filter Synthesis*. New York: Wiley, 1967.
[30] S. Bouwstra and B. Geijselaers, "On the resonance frequencies of microbridges," in *6th Int. Solid-State Sensors Actuators Conf. Tech. Dig.*, San Francisco, CA, June 24–27, 1991, pp. 538–542.
[31] Q. Meng, M. Mehregany, and R. L. Mullen, "Theoretical modeling of microfabricated beams with elastically restrained supports," *J. Microelectromech. Syst.*, vol. 2, no. 3, pp. 128–137, Sept. 1993.

[32] H. Nathanson, W. E. Newell, R. A. Wickstrom, and J. R. Davis, Jr., "The resonant gate transistor," *IEEE Trans. Electron Devices*, vol. ED-14, pp. 117–133, Mar. 1967.

[33] C. T.-C. Nguyen, "Micromechanical filters for miniaturized low-power communications," *Proc. SPIE*, to be published.

[34] V. B. Braginskky, V. P. Mitrofanov, and V. I. Panov, *Systems with Small Dissipation*. Chicago, IL: Univ. Chicago Press, 1985.

[35] K. Wang, A.-C. Wong, W.-T. Hsu, and C. T.-C. Nguyen, "Frequency-trimming and Q-factor enhancement of micromechanical resonators via localized filament annealing," in *Int. Solid-State Sensors Actuators Conf. Tech. Dig.*, Chicago, IL, June 16–19, 1997, pp. 109–112.

[36] K. Wang, Y. Yu, A.-C. Wong, and C. T.-C. Nguyen, "VHF free-free beam high-Q micromechanical resonators," in *12th Int. IEEE MEMS Conf. Tech. Dig.*, Orlando, FL, Jan. 17–21, 1999, pp. 453–458.

[37] C. T.-C. Nguyen, "Micromechanical signal processors," Ph.D. dissertation, Dept. Elect. Eng. Comput. Sci., Univ. California at Berkeley, Dec. 1994.

Clark T.-C. Nguyen (S'90–M'93) was born in Austin, TX, on March 29, 1967. He received the B.S., M.S., and Ph.D. degrees from the University of California at Berkeley, in 1989, 1991, and 1994, respectively, all in electrical engineering and computer sciences.

In 1995, he joined the faculty of The University of Michigan at Ann Arbor, where he is currently an Assistant Professor in the Department of Electrical Engineering and Computer Science. From 1995 to 1997, he was a member of NASA's New Millennium Integrated Product Development Team on Communications, which roadmaps future communications technologies for NASA use into the turn of the century. His research interests focus upon microelectromechanical systems, including integrated micromechanical signal processors and sensors and merged circuit/micromechanical technologies, RF communication architectures, and integrated circuit design and technology.

Prof. Nguyen received the 1938E Award for Research and Teaching Excellence from The University of Michigan at Ann Arbor in 1998, an EECS Departmental Achievement Award in 1999, and was a finalist for the 1998 Discover Magazine Technological Innovation Awards. Together with his students, he received the Roger A. Haken Best Student Paper Award at the 1998 IEEE International Electron Devices Meeting, and the Judges Award for Best Paper at the 1998 IEEE Microwave Theory and Techniques Society (MTT-S) International Microwave Symposium. He is currently the co-chairman of the Workshop on Microelectromechanical Devices for RF Systems at the 1999 IEEE MTT-S Symposium.